

1 **Identification of plasma environments within the
2 terrestrial magnetotail and its global structure from
3 the Magnetospheric Multiscale Mission**

4 **T. Vo^{1,3}, R. E. Ergun^{1,2}, M. E. Usanova¹, and A. Chasapis¹**

5 ¹ Laboratory for Atmospheric and Space Physics, University of Colorado, Boulder, CO, USA

6 ² Department of Astrophysical and Planetary Sciences, University of Colorado, Boulder, CO, USA

7 ³ Department of Physics, University of Colorado, Boulder, CO, USA

8 **Key Points:**

- 9
- 10 • Inner-magnetotail environments are statistically identified with background plasma conditions and their global 3D structure is studied.
 - 11 • Warping effects attributed to changes in the Earth's dipole tilt angle leads to an apparent dawn-dusk asymmetry during the summer months.
 - 12 • We utilize a large volume of MMS data with partial plasma moments calculated from low-energy plasma and energetic particle instruments.

15 **Abstract**

16 Using MMS orbits in the Earth's magnetotail from 2017 to 2020, plasma conditions
 17 and the 3D spatial structure of inner-magnetotail plasma environments (with a focus on
 18 the plasma sheet) are studied with different approaches. Threshold conditions for dis-
 19 tinguishing the plasma sheet, plasma sheet boundary layers, and lobes are derived from
 20 the statistical properties of background plasma parameters. Our results support previ-
 21 ous studies that employed similar methods using Cluster data. However, stronger cur-
 22 rents are observed in both the lobes and plasma sheet, likely due to the smaller space-
 23 craft separation ($\lesssim 70$ km) that can resolve thin electron-scale currents. Threshold con-
 24 ditions are used together with magnetic field and electric field measurements to image
 25 the spatial structure of the plasma sheet. Results are in good agreement with a global
 26 neutral sheet model based on solar wind conditions and magnetospheric configurations.
 27 Furthermore, the Earth's dipole tilts towards the Sun around June solstice, which warps
 28 the magnetotail as much as $\sim 2\text{--}4 R_E$ in Z GSM. This warping effect is relaxed towards
 29 September equinox. Consequently, as MMS travels through the magnetotail from dawn
 30 to dusk during this period, there is an apparent dawn-dusk asymmetry in plasma con-
 31 ditions between June and September. Kink-like flapping waves and IMF twisting are other
 32 mesoscale processes attributed with a few R_E of flaring near the flanks. These findings
 33 reveal important insights into the mesoscale structure and dynamics of the magnetotail.

34 **Plain Language Summary**

35 Data from four years of observations by NASA's MMS mission are used to statis-
 36 tically identify distinctive regions within the Earth's magnetospheric tail. This study re-
 37 veals insights into the spatial structure of this "magnetotail" and seasonal variations at-
 38 tributed with changes in the Earth's magnetic field configurations, particularly those of
 39 the orientation of the Earth's dipole. Our results agree with reported findings from ESA's
 40 Cluster mission. However, certain aspects unique to MMS lead to some improved mea-
 41 surements and features relating to MMS orbital design. The presented results are highly
 42 beneficial to future large statistical studies with MMS data.

43 1 Introduction

44 Situated at the nightside of the Earth's magnetosphere, the magnetotail can stretch
 45 as far as $\sim 10^3$ Earth radii (R_E) (Dungey, 1965; Cowley, 1991) and can exceed $30 R_E$
 46 in radius (Coroniti & Kennel, 1972; Shukhtina et al., 2004). Driven by interactions with
 47 the solar wind and the interplanetary magnetic field (IMF) as well as changes in geo-
 48 magnetic configurations and plasma conditions, it plays a central role in magnetospheric
 49 dynamics from global to kinetic scales. Therefore, to understand the multiscale dynam-
 50 ics within the magnetotail, there has been great interest to identify its complex struc-
 51 ture and plasma conditions.

52 From global to meso-scales, the magnetotail is subjected to distinct types of de-
 53 formation, three of which are known as flapping, twisting, and warping (Dayeh et al.,
 54 2015). Solar wind directional changes can cause it to flap either steadily in the north-
 55 south direction, or drive kink-like waves propagating towards the flanks (Lui et al., 1978;
 56 Sergeev et al., 2003; Zhang et al., 2005; Gao et al., 2018). The flapping and the waves
 57 have periods on the order of 1–10 minutes with wavelengths of 1–4 R_E (Rong et al., 2018;
 58 Wang et al., 2019). Non-zero IMF B_y can apply a torque and twist the tail as high as
 59 50° about the Sun-Earth line (Owen et al., 1995; Tsyganenko, 1998). Due to the $\sim 11^\circ$
 60 tilt of the Earth's dipole axis with respect to its rotational axis (Amit & Olson, 2008),
 61 the magnetotail is periodically displaced $\sim 1\text{--}2 R_E$ above and below the equatorial plane
 62 (Hammond et al., 1994) with a hinge radius of $\sim 10 R_E$ (Tsyganenko & Fairfield, 2004).
 63 Under these effects, the tail shape is extremely complex and variable on time scales from
 64 a few minutes to many days and spatial scales up to many Earth radii.

65 There are several distinct plasma environments in the magnetotail. Boundary lay-
 66 ers at the flanks can bring magnetosheath plasma into the inner magnetosphere via mix-
 67 ing instabilities (e.g. Otto & Fairfield, 2000; Fairfield et al., 2000; Nykyri et al., 2006;
 68 Johnson et al., 2014). In the middle of the tail, a plasma sheet (PS), which is a few R_E
 69 in thickness under normal conditions (Russell & McPherron, 1973; McComas et al., 1986;
 70 Sanny et al., 1994; Zhou et al., 1997), contains high-beta plasma and low equatorial mag-
 71 netic field (Baumjohann et al., 1989). To the contrary, the northern and southern lobes
 72 enclosing the PS are often characterized by low-beta plasma and high equatorial mag-
 73 netic field, predominantly pointing sunward or antisunward. Separating the PS and the
 74 lobes, the plasma sheet boundary layers (PSBLs) mix hot and cold plasmas from these

two environments (Eastman et al., 1984) and often display signatures of nonlinear kinetic structures (Cattell et al., 1986; Nakamura et al., 2004; Ergun et al., 2009; Malaspina et al., 2015; Tong et al., 2018). Embedded within the PS is a neutral sheet (NS), often characterized as the null point of the equatorial magnetic field. The NS is the locus of many explosive geomagnetic activities during substorms (Sitnov et al., 2019, and references therein) which include, for example, kinetic instabilities, magnetic reconnection, locally generated turbulence, particle energization, etc (Zimbardo et al., 2010; Sitnov & Schindler, 2010; Liu et al., 2014; Ukhorskiy et al., 2017; Chen et al., 2019; Ergun et al., 2020a, 2020b, 2022; Usanova & Ergun, 2022).

The complex evolution of mesoscale dynamics and kinetic-scale structures often make identifying the various plasma environments a non-trivial task. Previous attempts to identify plasma environments and their spatial variations in the inner magnetotail have included a number of different methods. Combining decades of data, multi-mission studies (Hammond et al., 1994; Tsyganenko & Fairfield, 2004; Dayeh et al., 2015; Xiao et al., 2016) have imaged the neutral sheet under twisting and warping effects by observing the sign of magnetospheric B_x , from which global models are constructed. Multi-spacecraft missions, e.g. Cluster (Escoubet et al., 2001) and THEMIS (Angelopoulos et al., 2008), allow for timing analysis, often used to study the flapping motion (Runov et al., 2005, 2009). Most commonly, statistical threshold conditions based on averaged background parameters such as the plasma beta, number density, current density, magnetic field and/or plasma flow are used to distinguish the NS, PS, PSBL, and lobe (Baumjohann et al., 1988; Angelopoulos et al., 1994; Åsnes et al., 2008; Boakes et al., 2014). Assuming a certain time scale of the magnetic fluctuations, threshold conditions can also be defined based on magnetometer data alone to distinguish the lobe and PS (Coxon et al., 2016). When the threshold approach fails, the outer layer of the PS and PSBL may be determined on a case-by-case basis by analyzing beam-like populations in the 3D distribution function (Grigorenko et al., 2012) or ionospheric photoelectrons (Pedersen et al., 1985; Baumjohann et al., 1988).

The Magnetospheric Multiscale mission (MMS), launched in 2015, is a NASA four-spacecraft mission (Burch et al., 2016) that targets electron-scale magnetospheric physics, building upon the success of Cluster. Capable of higher time resolution and higher accuracy electromagnetic field and particle measurements, MMS has the potential to reinforce past studies of global models, threshold conditions, and kinetic-scale properties.

108 As apparent from previous experiences, it is challenging to achieve a definitive identi-
109 fication of the inner-magnetotail plasma environments at any given time. Nevertheless,
110 knowledge of mesoscale factors and background parameters from MMS data can provide
111 insights into the magnetotail configuration at various scales. We remark that identify-
112 ing plasma regions and boundaries is essential to a systematic statistical study of kinetic-
113 scale magnetotail physics.

114 In this paper, we utilize a large volume of MMS observations to investigate the prop-
115 erties of magnetotail plasma environments through a few different approaches, with a
116 focus on the plasma sheet. Statistically, we derive threshold conditions based on back-
117 ground plasma conditions to distinguish different environments. Results are discussed
118 in comparison with those from a previous study using Cluster data (Boakes et al., 2014).
119 Furthermore, the large volume of data allows for enough spatial coverage to image the
120 global structure of the neutral sheet (i.e. through magnetic field measurements similar
121 to Tsyganenko & Fairfield, 2004; Xiao et al., 2016). The structure of the NS based on
122 B_x will be compared with that of the PS identified from the threshold approach, and
123 the NS model fitted by Xiao et al. (2016). Since the NS is embedded within the PS, we
124 show that all of these approaches (threshold, imaging, modeling) generally agree, thereby
125 revealing insights into both the statistical properties of background plasma conditions
126 and the spatial variations of the NS/PS within the magnetotail. For example, since MMS
127 always visits the magnetotail from June solstice to September equinox (correspondingly,
128 from the dawn to dusk sectors in GSM coordinates), observations of the PS spatial struc-
129 ture reveal that warping effects are prominent around June and insignificant around Septem-
130 ber, resulting in an apparent dawn-dusk asymmetry in plasma conditions. Our data also
131 feature the combination of partial plasma moments from low-energy plasma and ener-
132 getic particle instruments, the technicality and motivation for which are presented in this
133 paper.

134 This paper is organized as follows. In Section 2, we describe relevant details of MMS
135 instrumentation. In Section 3, we describe our dataset, which is compiled from a broad
136 array of MMS instruments measuring fields and particles, where we also present the com-
137 bined plasma moments and the motivation for their consideration. In Section 4, we dis-
138 cuss the exclusion of outer magnetotail environments and present the properties of back-
139 ground plasma conditions in the inner magnetotail. In Section 5, we examine the 3D global
140 structure of the neutral sheet and plasma sheet using the threshold, imaging, and mod-

¹⁴¹ eling approaches. Finally, we discuss the implications of these results and provide con-
¹⁴² cluding remarks in ??.

¹⁴³ **2 Instrumentation**

¹⁴⁴ A broad array of MMS instruments are used enable and optimize statistical mag-
¹⁴⁵ netotail studies of the electromagnetic field, particle properties, and their correlation. While
¹⁴⁶ the present paper only concerns with statistical, mesoscale quantities, we recognize that
¹⁴⁷ the large volume of data considered here also can be generically advantageous for future
¹⁴⁸ large-scale studies of kinetic physics in the magnetotail.

¹⁴⁹ The four identical MMS spacecrafts travel in a tetrahedral formation with a highly
¹⁵⁰ eccentric, near-Earth-equatorial orbit with an initial apogee of $12 R_E$ and a perigee of
¹⁵¹ roughly $1.2 R_E$ (Fuselier et al., 2016). The natural (inertial) orbital precession is small,
¹⁵² but as the Earth orbits the Sun, the apogee rotates between the subsolar region and the
¹⁵³ magnetotail in roughly one year. Annually, magnetotail observations occur for MMS pri-
¹⁵⁴ marily in the summer months between June solstice and September equinox. To max-
¹⁵⁵ imize encounters with the neutral sheet during these seasons, the night-side apogee was
¹⁵⁶ raised to $25 R_E$ in early 2017 and subsequently to $28 R_E$ in 2019 (Tedla et al., 2018). Through-
¹⁵⁷ out the magnetotail, MMS instruments operate in two data acquisition rates (fast sur-
¹⁵⁸vey and burst). Fast survey data provide continuous coverage, and burst data are se-
¹⁵⁹lected short-duration intervals of high time-resolution measurements. In this paper, we
¹⁶⁰ use fast survey data from 2017 to the end of 2020 to optimize statistical observations of
¹⁶¹ magnetotail processes occurring between 12 and $28 R_E$.

¹⁶² In fast survey mode, the FIELDS investigation provides measurements of the DC
¹⁶³ magnetic field and DC electric field in resolutions of 62.5 ms and 31.25 ms through the
¹⁶⁴ Fluxgate Magnetometers (FGM) and Electric Double Probes (EDP) instruments (Torbert
¹⁶⁵ et al., 2016; Russell et al., 2016; Ergun et al., 2016). At apogee, the tetrahedral forma-
¹⁶⁶ tion is targeted to have a geometric quality factor $Q \geq 0.7$ ($Q = 1$ being a perfect tetra-
¹⁶⁷hedron) and an average spacecraft separation of 40 km, enabling measurements of field
¹⁶⁸ gradients on several electron scales (Fuselier et al., 2016). Particularly, the current den-
¹⁶⁹ sity $\mathbf{J} = \nabla \times \mathbf{B}/\mu_0$ can be estimated using the curlometer technique (Paschmann & Daly,
¹⁷⁰ 1998; Dunlop et al., 2021). Simultaneous multi-spacecraft measurements also allow for
¹⁷¹ calculations of barycentric quantities so that, for example, plasma dissipation measures

such as $\mathbf{J} \cdot (\mathbf{E} + \mathbf{u} \times \mathbf{B})$ (Zenitani & Hoshino, 2005; Ergun et al., 2018) or $(\mathbf{P} \cdot \nabla) \cdot \mathbf{u}$ (Chasapis et al., 2018; Yang et al., 2022) may be examined.

The Fast Plasma Investigation (FPI) samples plasma populations in the low-energy range from 10 eV to 30 keV with time resolutions of 30 ms for electrons and 150 ms for ions (Pollock et al., 2016). FPI instruments utilize top-hat electrostatic analyzers, forming 512 distributed field-of-views (FOVs) over the full 4π -sr solid angle, each measuring 32 energy channels. The fast survey FPI data products used in this study are 3D electron and ion distribution functions that are integrated on-board high time-resolution measurements and reduced to 4.5-s resolution. FPI also provides partial plasma moments (associated with its capable energy range) integrated in velocity space from the 4.5-s products.

At the high-energy range, the Energetic Particle Detector (EPD) investigation comprises the Fly's Eye Energetic Particle Sensor (FEEPS) and Energetic Ion Spectrometer (EIS) instruments, utilizing micro-channel plates and solid-state detectors to sample energetic particles in the range of 60–500 keV (Mauk et al., 2016; Blake et al., 2016). For better ion data availability and energetic electron measurements, we utilize FEEPS data in this study. On each spacecraft, two FEEPS instruments are mounted 180° apart on the spin plane, providing 9 electron FOVs (5 operating in fast survey) and 3 ion FOVs, each measuring energy with 16 channels. Although this configuration provides instantaneous measurements of the particle distribution over a 3π -sr solid angle, the main data products are electron and ion energy-angle distributions, averaged in 2.5-s resolution by means of rotation. As opposed to the full 3D distribution functions measured by FPI at low energies, the most reliably available of the FEEPS measurements are spin-scanned, omni-directional distribution functions. Therefore, the partial plasma moments that can be calculated from FEEPS data are more limited than those from FPI data.

3 Methodology and Data

In the previous section, it is clear that low-energy ($\lesssim 30$ keV) and high-energy ($\gtrsim 60$ keV) particles are measured by MMS with instruments that have quite distinct techniques (FPI and FEEPS, respectively), resulting in different time resolutions, angular coverages, and an energy-coverage gap of about 30 keV. Therefore, it is not trivial how partial plasma moments may be calculated (in the high-energy range) and combined from

the two instruments. While the combination of partial plasma moments has been applied for previous capable missions such as THEMIS (Angelopoulos et al., 2008; Hietala et al., 2015; Shustov et al., 2019) and Cluster (Haaland et al., 2010), it has not been routinely performed for MMS and is often the constraining factor in previous studies, particularly those investigating ion properties. For example, Artemyev et al. (2021) acknowledges the importance of contributions of 100-keV ions to the plasma moments in the magnetotail, but because of the aforementioned constraint, these contributions are extrapolated using THEMIS data by a scaling argument instead of direct calculations. In the following, we provide another motivation for the necessity of combined plasma moments in the magnetotail through a case study. At the same time, we present a demonstration of our methodology in estimating the contributions of energetic particles to the plasma moments. Technical details of this combination are specific to MMS data products and discussed at length in ??.

Consider a well-documented observation of a strongly turbulent, retreating reconnection X-line in the magnetotail in Fig. 1 (Ergun et al., 2018, 2020a, 2020b). In (a–c), an ion flow reversal occurs around 07:29, together with strong electromagnetic fluctuations persisting about 15 minutes, in which many intermittent structures are found such as double layers, magnetic holes, electron phase-space holes, and thin current sheets. At the same time, increases in energetic ion and electron numberenergy fluxes are observed in (d) and (e). The numberenergy fluxes at some time before, during, and after the turbulent event (denoted in (a–h) with vertical blue, green, and red lines) are also plotted in (i) and (j). The particle distributions in (d–e) and (i–j) are omni-directional and contain both measurements from FPI (below the lower-energy, magenta dashed line) and FEEPS (above the higher-energy dashed line). Since FPI has lower time resolution, FEEPS measurements are interpolated to FPI resolution.

From past statistical studies (Huang et al., 2020; Chong et al., 2022), it is reasonable to assume that the plasma bulk flow rarely surpasses FPI capabilities (about 2,000 km/s for ions and 100,000 km/s for electrons). So the contribution from thermal (low-energy) particles to the plasma moments can be calculated from the FPI 3D distribution functions, correctly accounting for drifted particles. Subsequently, the non-thermal contribution may be considered isotropic and calculated from omni-directional distribution functions as detailed in ?. However, this calculation is limited to directionless quantities, such as the number density and scalar pressure. Most clearly seen in (i–j), the energy-

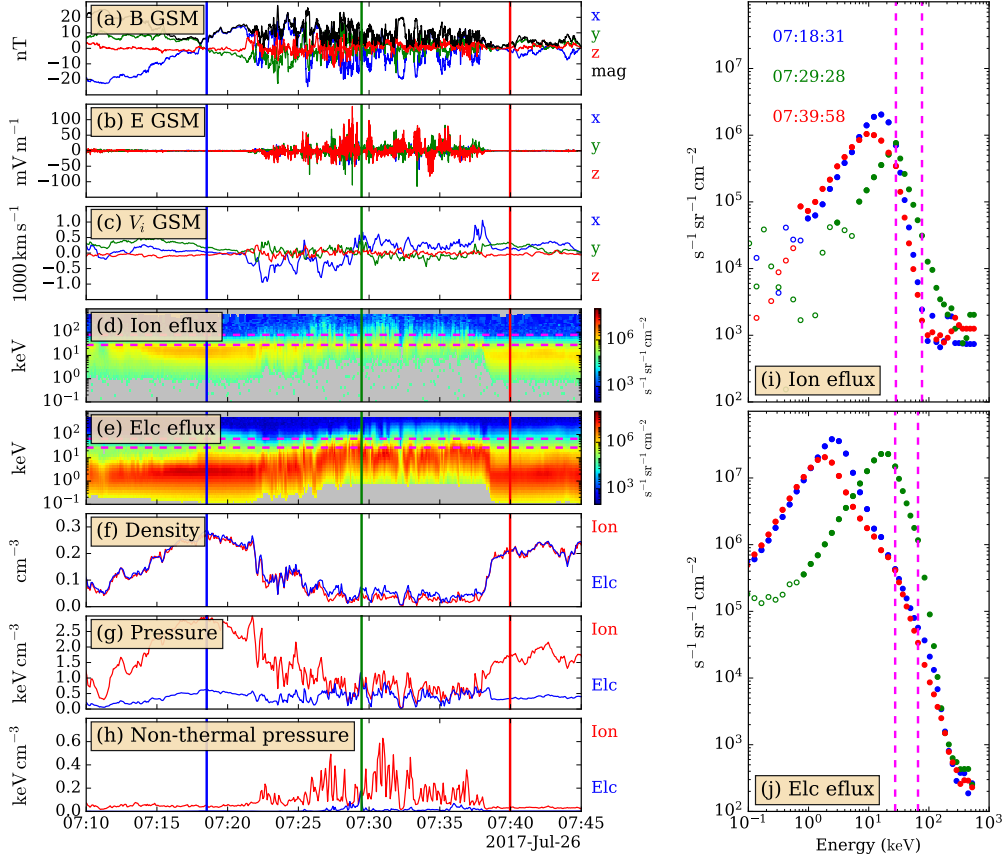


Figure 1. Example of FPI-FEEPS combined moment calculations for a strong turbulent reconnection event in the magnetotail. (a) Barycentric magnetic field. (b) Barycentric electric field. The rest of the panels show data from MMS1. (c) Ion velocity. (d) Combined omni-directional ion [numberenergy](#) flux. (e) Combined omni-directional electron [numberenergy](#) flux. (f) Combined ion (red) and electron (blue) density. (g) Combined ion and electron total pressure. (h) Pressure contribution of non-thermal, energetic (larger than FPI energy threshold) particles. In (a-h), the blue, green, red vertical lines are times before, during, and after the turbulent event. (i) The ion [numberenergy](#) flux during vertical snapshots in (a-h). (j) Similarly, snapshots in electron [num-](#)
[berenergy](#) flux. [Hollow markers are noise-level or background measurements.](#) The dashed magenta lines [horizontal in (d) & (e), vertical in (i) & (j)] denote the extrapolated energy gap between FPI and FEEPS. There are 5 extrapolated points in that gap.

coverage gap (between the dashed lines) may contain a significant contribution to the plasma moments. Thus, we extrapolate the distribution function in this gap from FPI and FEEPS measurements and include its contribution in the non-thermal moment calculations (see ??). In (f–h), we show the total (thermal + non-thermal) number density, total pressure, and non-thermal pressure.

In this event, one significant feature emphasized by the Ergun et al studies is that the reconnection inflow does not resupply particles from the lobe as fast as plasma sheet particles are depleted by the outflow, which results in a density drop in the turbulent region in (f) and the depletion of low-energy particles in (i–j). What we emphasize here is that because of this depletion of low-energy particles, when comparing (g) and (h), the contribution of non-thermal and/or energetic ions to the total pressure (characteristic energy density $P_s = nk_B T_s$ of species s) is on the order of 10 % and can be as high as 50 %. While most electrons are within the thermal (FPI) energy range, there can also be a significant fraction of non-thermal electrons ($\sim 10\text{--}20\%$ of total electron pressure) in this type of events. Since the frequency of events similar to the one shown in Fig. 1 is not yet established, pressure and temperature calculations solely based on the FPI instrument in the magnetotail may be underestimated for these occurrences. Therefore, it may be crucial for statistical studies of particle energization in the magnetotail to consider plasma moments combined from both FPI and FEEPS.

The calculation of combined plasma moments above requires that there is simultaneous availability from both particle instruments. We also require that electromagnetic field observations (from FGM and EDP) are available to enable future statistical studies of the correlation between field and particle observations. Such a study will be able to establish the statistical occurrence between turbulence, reconnection, and particle energization events such as the example in Fig. 1.

For this study, we have compiled continuous intervals (no significant time gap; duration from minutes to hours) of good availability from the magnetic field, electric field, low-energy plasma, and energetic particle instruments during MMS magnetotail seasons from 2017 to 2020. Additionally, 1-minute averaged solar wind conditions are obtained from the OMNI dataset (King & Papitashvili, 2005), which is used to correlate the magnetotail dynamics with solar wind conditions. In total, there are 437,728,300 field (FGM resolution) and 6,078,827 particle (FPI resolution) data points, amounting to about 316

268 continuous days of observation. Details of compilation of these intervals are highly tech-
 269 nical and are laid out in the Supporting Information (SI). The principal conditions are
 270 listed below.

- 271 1. $X < 0$
- 272 2. $R \geq 12R_E$
- 273 3. $Q \geq 0.75$
- 274 4. No periods of thruster firing, EDP probe saturation, shadow spikes, or bad bias
 settings.
- 275 5. FGM, EDP available from MMS(1–4).
- 276 6. FPI, FEEPS available from MMS1.
- 277 7. Interval at least 1-minute long.

279 Above, $\mathbf{R} = (X, Y, Z)$ is the spacecraft position in GSM. While most global models of
 280 the neutral sheet, one of which is later on analyzed and compared, are fitted in aberrated
 281 GSM (AGSM), we have found little difference between GSM and AGSM in our results.
 282 Thus, we retain the usage of GSM for all coordinates in subsequent sections. Conditions
 283 (3) and (5) ensures that the barycentric electromagnetic fields and the curlometer cur-
 284 rent density may be accurately estimated. (4) ensures intervals of adequate EDP data
 285 for analysis. (6) ensures the partial plasma moments can always be combined. (7) en-
 286 forces that the intervals are adequately long for spectral analysis.

287 4 Properties of the magnetotail background plasma conditions

288 In this section, we first distinguish the inner magnetotail from the solar wind and
 289 flank-side boundary layers, the properties of which are outside the scope of the present
 290 paper. Then, we present the statistical properties of the inner-magnetotail plasma con-
 291 ditions and compare our results with those in Boakes et al. (2014), hereby referred to
 292 as B14. Also, as done in B14, threshold conditions for the PS, PSBL, and lobe are de-
 293 rived based on the statistical properties of the plasma.

294 4.1 Exclusion of solar wind and flank-side boundary layers

295 Fig. 2 shows the X – Y distribution of (a) the coverage of MMS trajectory, (b) the
 296 ion density n_i , (c) the electron temperature T_e , and (d) the standard deviation of the

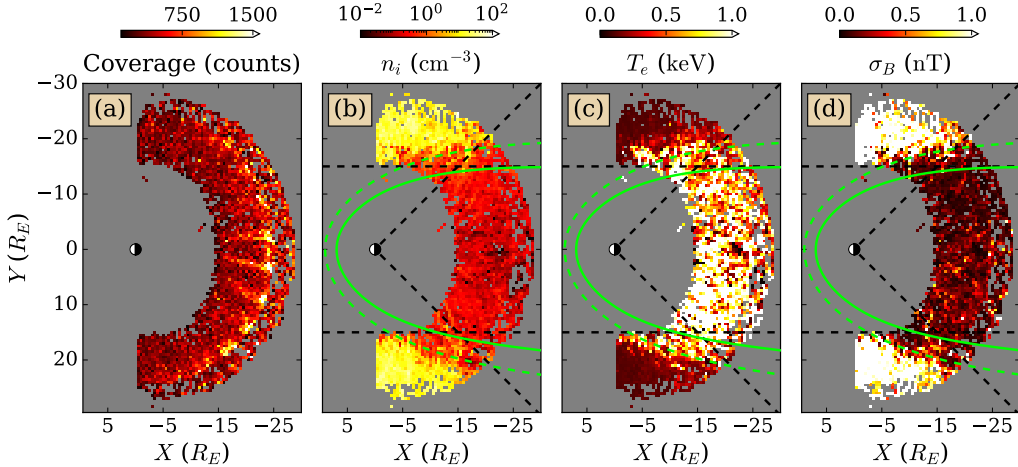


Figure 2. Spatial distribution in the X - Y plane of (a) MMS coverage during tail seasons in 2017–2020, (b) the ion density n_i , (c) the electron temperature T_e , and (d) standard deviation of the magnetic field σ_B . The lime curves are a 5° (clockwise) tilted magnetopause model (Lin et al., 2010) constructed with zero IMF B_z and total solar wind pressure of 5 nPa (dashed) and 20 nPa (solid). Dashed black lines denote $|Y| \leq 15 R_E$ and $|Y| \leq |X|$. The color scales are chosen to saturate solar wind values to also reveal typical plasma values in the tail.

297 magnetic field σ_B (over a 5-s moving window). In the magnetotail, the electron density
 298 (n_e) measurement is more accurate than n_i . However, the reverse is true in the solar wind.
 299 Here, we use n_i to reveal the differences between the solar wind and the magnetotail.
 300 Later, we use n_e when characterizing the magnetotail. 3D histograms are calculated with
 301 $0.5 R_E \times 0.5 R_E \times 0.5 R_E$ cubic bins then averaged over the Z direction, except for (a),
 302 which is summed instead. Hereafter, all data (e.g. the magnetic field, electric field, and
 303 current density) are averaged over a 5-s moving window and subsequently down-sampled
 304 to FPI resolution (4.5 s) so that particle and field measurements can be compared. Thus,
 305 in (a), each count represents a 5-s observation and the total count in each bin represents
 306 the dwell time of MMS spacecrafts. 3D bins that have lower than 100 counts are excluded
 307 as they may not be statistically representative.

308 In (a), the dwell time is not uniform. The highly-eccentric orbit has MMS spend
 309 more time near the apogee to maximize the chance of observing the diffusion region at
 310 reconnection sites (Fuselier et al., 2016). However, bins that have statistically significant
 311 counts are distributed over a large and uniform enough area so that the spatial distri-

bution of plasma parameters can be studied. Most notably in (b–d), the solar wind is observed (as saturated colors) at $|Y| \gtrsim 15 R_E$, where averaged values are $n_i \sim 10\text{--}100 \text{ cm}^{-3}$, $\sigma_B \sim 1\text{--}5 \text{ nT}$, and $T_e \sim 0.01\text{--}0.1 \text{ keV}$. In contrast, plasma parameters in the inner magnetotail are generally 1–2 orders of magnitude smaller, where $n_i \sim 0.1\text{--}1 \text{ cm}^{-3}$, $\sigma_B \sim 0.1\text{--}0.5 \text{ nT}$, and $T_e \sim 1 \text{ keV}$. [This figure](#)[Fig. 2](#) shows that in general, background plasma parameters such as the density, temperature, and magnetic field fluctuations are distinctive between the inner and outer magnetotail. Thus, we can use these differences to statistically exclude regions more likely associated with the solar wind or flank-side boundary layers.

OMNI solar wind observations during MMS magnetotail seasons indicate average IMF $B_z \sim 0$ and total pressure $P_{\text{sw}} \sim 1\text{--}5 \text{ nPa}$. We use these parameters to construct an asymmetric magnetopause model (Lin et al., 2010), plotted as dashed ($P_{\text{sw}} = 5 \text{ nPa}$) and solid ($P_{\text{sw}} = 20 \text{ nPa}$) lime curves in (b–d). Details about the average OMNI observations and the Lin10 model are provided in ???. The dashed curve agrees well with the change in plasma parameters. Thus, to be conservative when eliminating boundary layers, we define the inner magnetotail as the region bounded by the solid lime curve. In subsequent sections, all statistical results are obtained with data located strictly within this region.

For comparison, previous statistical studies have typically constrained the inner magnetotail region either with (i) $|Y| \leq |X|$ (Ergun et al., 2015) or (ii) with a threshold $|Y| \leq Y_0$ (Boakes et al., 2014; Chong et al., 2022). These two constraints are plotted as dashed black lines in (b–d). On a closer look, they are all somewhat equivalent conditions. (i) tends to work for smaller radial distances $R \leq 12 R_E$, and (ii) is good for small enough threshold Y_0 , although the popular choice $Y_0 = 15 R_E$ may include some mixed plasma data.

4.2 Identification of inner tail plasma environments

Fig. 3 shows the statistical profile of background plasma parameters in terms of the ion beta $\beta_i = P_i/(B^2/2\mu_0)$, where P_i is the ion pressure. For comparison, it is plotted in the same format as Figure 1 in B14. (a) and (b) show the current density components parallel (J_{\parallel}) and perpendicular (J_{\perp}) to the background magnetic field. (c) shows the electron density n_e , and (d) shows the equatorial magnetic field B_{xy} . [Similar to Fig. 2\(a\)](#),

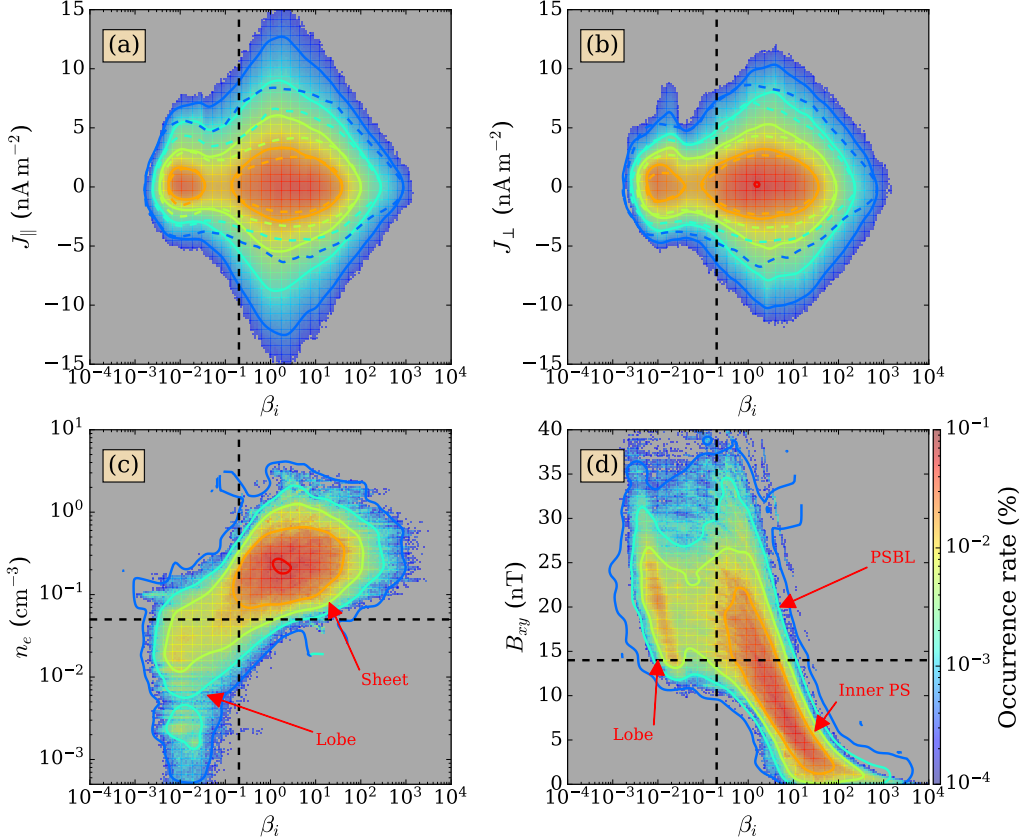


Figure 3. Statistical distribution Occurrence rates of (a) the parallel current density J_{\parallel} , (b) the perpendicular current density J_{\perp} (in the cross-tail direction, $\hat{\mathbf{z}} \times \mathbf{B}$), (c) the electron density n_e , and (d) the equatorial magnetic field B_{xy} in terms of the ion plasma beta β_i . Solid lines are contours of the colored distributions. In (a) and (b), the overplotted colored dashed lines are contours of the noise estimation of the curlometer current, $\nabla \cdot \mathbf{B}/\mu_0$. In all panels, the vertical dashed line denotes $\beta_i = 0.2$. In (c), the horizontal dashed line is the FPI 1-count level $n_e = 0.05 \text{ cm}^{-3}$. In (d), the horizontal dashed line denotes $B_{xy} = 14 \text{ nT}$. The current and magnetic field measurements are down-sampled to FPI resolution in this figure.

Table 1. Threshold conditions distinguishing tail plasma environments derived from Fig. 3.

Plasma environment	Condition
Lobe	$\beta_i < 0.2$
Plasma sheet	$\beta_i \geq 0.2 \text{ \& } B_{xy} \leq 14 \text{ nT}$
Plasma sheet boundary layer	$\beta_i \geq 0.2 \text{ \& } B_{xy} > 14 \text{ nT}$

each count represents a 5-s observation. Due to the solenoidal condition ($\nabla \cdot \mathbf{B} = 0$), the noise level of the curlometer currents in (a–b) can be estimated as $J_{\text{noise}} = \nabla \cdot \mathbf{B}/\mu_0$. In these panels, we have overplotted the contours of J_{noise} for comparison with the current amplitude. At a given color, currents larger than noise are measured if the solid line is wider than the dashed line.

In general, the features in this plot are consistent with the Cluster study. Most clearly in all panels, there are two distinct populations separated by β_i . The lobe-like population has low density ($n_e \sim 0.01 \text{ cm}^{-3}$), low beta ($\beta_i \sim 0.01$), and high equatorial magnetic field ($B_{xy} \sim 20 \text{ nT}$). In contrast, the plasma sheet-like population has high density ($n_e \sim 0.1 \text{ cm}^{-3}$), high beta ($\beta_i \sim 1$), and low field ($B_{xy} \sim 5 \text{ nT}$). One note of caution is the region of low electron density. The FPI instrument has a large uncertainty if the electron density is below 0.05 cm^{-3} [horizontal dashed line in (c)]. However, noise and background in the combined FPI-FEEPS distribution function has been treated carefully in the low-density region such that the accuracy is improved (see ?? for details). In subsequent sections, the threshold conditions for the plasma sheet are the main subject of study, where the density is typically higher than this the FPI threshold. While it is possible that there are unusually low-density plasma in the PS, such as a few data points during the turbulent event in Fig. 1, the occurrence is brief and does not significantly alter the results of a large statistical study.

To systematically determine the thresholds, B14 used changes in the current and electron densities with respect to β_i to define the PS/lobe separation and similarly, the statistical spread in B_{xy} to distinguish between the PSBL and the outer/inner regions of the plasma sheet. The threshold conditions were then reported annually. However, we deem it unnecessary for that level of detail in this study. It suffices to define by visual inspection the threshold conditions as tabulated in Table 1 and annotated in Fig. 3.

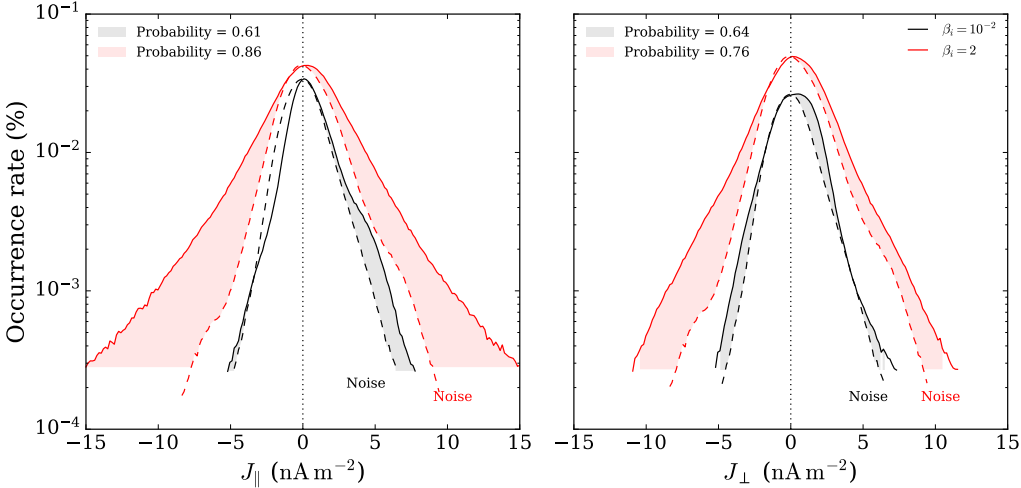


Figure 4. Vertical cuts of the statistical distribution of the currents in Fig. 3(a–b) at $\beta_i = 10^{-2}$ (in black) and $\beta_i = 2$ (in red). The corresponding dashed lines with the same colors are the noise estimation J_{noise} . The shaded areas are those where more occurrence is observed at a given amplitude than the noise estimation. The probability of these observations based on the shown conditional distribution functions (on β_i) is provided in the legends (shaded area versus total area under the solid lines).

We also make no attempt to distinguish the inner PS from the outer PS as done in B14. In general, our thresholds are all consistent with averages from the yearly results in B14. The beta threshold is slightly higher (by a factor of 2), most probably due to the usage of combined plasma moments (only partial moments with energies $\lesssim 40$ keV were used in the B14 study).

A significant difference between our results and the B14 results is the current density. In (a) and (b), stronger currents ~ 1.5 – 5 nA/m 2 are observed, while the current amplitude in B14 is ~ 0.5 – 2 nA/m 2 . While B14 only observed noise level lobe currents ~ 0.1 nA/m 2 , this study reveals significant lobe currents with amplitude comparable to those in the PS and PSBL. Additionally, the parallel component in (a) averages to zero, indicating that the current frequently propagates obliquely with respect to the background magnetic field in both the lobe and PS. This also shows that the plasma is often frozen into the magnetic field. In (a) and (b), the average current amplitude in the PS is consistent with results in B14 (0.5–2 nA/m 2). However, a difference among our results is in the lobe (low-beta region). B14 only observed noise in this region ($J \sim 0.5$ nA/m 2). But the wider (green/blue) contours than J_{noise} show that there are

383 detections of statistically significant lobe currents above the noise level. To better visu-
 384 alize this difference, Fig. 4 shows vertical cuts of these panels at $\beta_i = 10^{-2}$ (black) and
 385 $\beta_i = 2$ (red). The occurrence rate of high-beta currents is higher than those with low
 386 β_i . The shaded regions indicate that there are “wings” in the probability distribution
 387 functions (PDFs) that is more significant than the statistics of noise (dashed lines).
 388 At any occurrence rate below $2 \times 10^{-3} \%$ for low β_i , the detected current amplitudes
 389 are higher than the estimated noise, which means wider contours in Fig. 3. Finally,
 390 to show the partition between noise-level currents (in the “core” of the PDFs) and
 391 non-noise currents (in the wings), we calculate the probability of the latter (see the
 392 figure legends) and discover that at least half of the observations are not noise. That
 393 said, the low overall occurrence rate indicates that their detection is not common.

394 ~~An explanation for the discrepancy in current amplitude lies in the average spacecraft separa-~~
 395 ~~tion.~~ In the magnetotail, the typical Cluster spacecraft separation is 1000s of km (Escoubet
 396 et al., 2001), which is comparable to the average ion inertial length. About $\sqrt{m_i/m_e} \sim 40$
 397 times smaller, the typical electron inertial length is ~ 20 km. Since the target of MMS
 398 is electron physics, 97 % of the dataset has spacecraft separation ≤ 70 km (not shown).
 399 As a result, intense electron-scale currents are resolved in MMS data, but may be un-
 400 derestimated in Cluster data due to the linear spatial interpolation in the curlometer tech-
 401 nique (Paschmann & Daly, 1998). ~~This can explain the higher average amplitude in MMS ob-~~
 402 ~~servations.~~ Therefore, we hypothesize that the presence of significant lobe currents in
 403 our statistics is due to the smaller spacecraft separation. Future studies are necessary to
 404 reveal their origin and properties. Overall, these results still provide strong support of
 405 Cluster observations from the MMS mission, with an improvement on current density
 406 measurements.

407 5 Global structure of the magnetotail plasma sheet

408 In this section, we investigate the three-dimensional global structure of the plasma
 409 sheet. As mentioned in Section 1, the magnetotail is influenced by processes such as flap-
 410 ping, twisting, and warping. Therefore, the plasma sheet may be highly deformed on mesoscales.
 411 In that case, it is interesting to study the spatial variations of the background plasma
 412 conditions, based on which the PS threshold condition is established in Table 1. From
 413 solar wind observations in ??, the average IMF B_y is around 2 nT with near-zero IMF
 414 B_z , suggesting that the twisting angle should not be significant for radial distances smaller

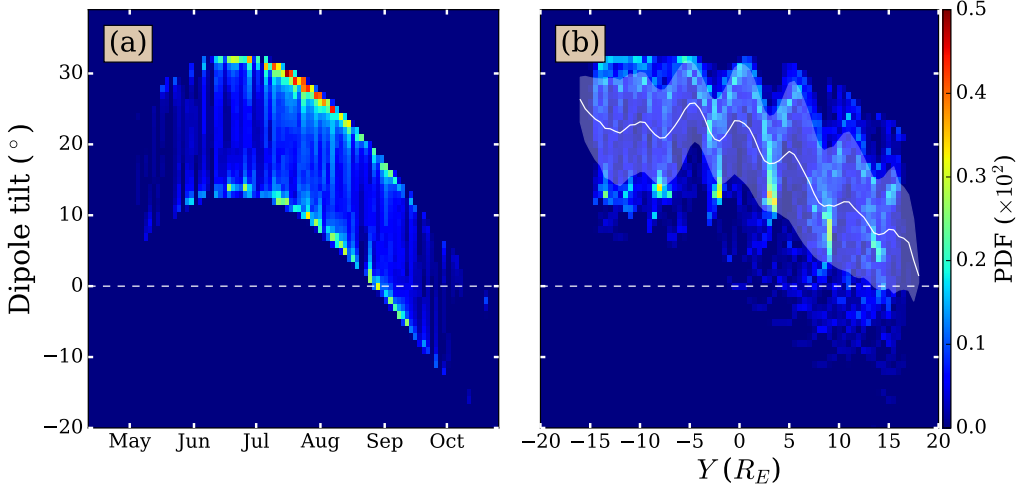


Figure 5. Distribution of the dipole tilt angle Ψ (a) in time and (b) in Y . The average Ψ is plotted as the solid white line in (b).

than $30 R_E$ (Tsyganenko & Fairfield, 2004), which leaves flapping and warping as the main deforming factors during MMS magnetotail seasons.

To investigate the warping of the magnetotail plasma sheet, we consider the Earth's dipole tilt angle Ψ obtained from the MMS Magnetic Ephemerides Coordinates (MEC) dataset generated by Henderson et al. (2018). In GSM coordinates, Ψ , constrained in the $X-Z$ plane, is the angle between the Earth's dipole tilt axis and the Z axis, which is positive when the Earth tilts toward the Sun and negative away from the Sun. Due to the daily Earth rotation, Ψ varies almost sinusoidally with an amplitude of about 10° and a period of about 1 day (not shown). Fig. 5 shows the distribution of Ψ with respect to (a) the time of year and (b) the concurrent MMS spacecraft position in Y .

In (a), there are two peaks separated by $\sim 20^\circ$ due to the daily variation of Ψ and the seasonal variation of the dipole tilt (Ψ is lower in October). The daily variation is also seen in panel (b). However, (b) also shows that Ψ is lower at higher Y . The correlation between Ψ and Y is due to low natural precession of the MMS orbit, which causes MMS to visit the magnetotail only in the summer months. In these seasons, MMS enters the magnetotail from the dawn-side flank ($Y \sim -15 R_E$) around May when Ψ is high and exits to the dusk-side flank ($Y \sim 15 R_E$) around October when Ψ is low. The solid white line in (b) shows the average value of Ψ in terms of Y , which is around 20° in the

433 dawn sector ($Y < 0$) and gradually decreases to zero in the dusk sector ($Y > 0$). The dif-
 434 ference in average Ψ between these two sectors can lead to significant variations as a func-
 435 tion of Y due to dipole tilt warping effects.

436 Using the same bin size as that in Fig. 2 ($0.5 R_E$), Figs. 6 and 7 show the spatial vari-
 437 ations of several background parameters in both the $X-Z$ and $Y-Z$ plane (the third dimension is
 438 averaged in both cases), thereby providing a 3D picture of these quantities. In Fig. 6, we show (a) the
 439 ion plasma beta β_i , (b) the equatorial magnetic field B_{xy} , and (c) the normal electric field E_z . Fig. 6
 440 shows the (Y averaged) spatial structure of (a) the ion plasma beta β_i , (b) the equato-
 441 rial magnetic field B_{xy} , and (c) the normal electric field E_z . Similarly, Fig. 7 shows the
 442 (X averaged) spatial structure of (a) B_x and (b) Ψ . The structures of these parameters
 443 altogether provide a 3D picture of the plasma sheet, with the tilt angle Ψ indicating
 444 the degree of warping.

445 In each panel Fig. 6 from (a) to (c), the bins are marked with a dot if they satisfy
 446 the beta condition, the magnetic field condition, and both (the plasma sheet condition
 447 in Table 1), respectively. The features in this figure correspond one-to-one with those
 448 discussed in Table 1. First, in Fig. 6(a), while constraining β_i to high values mostly ex-
 449 cludes environments consistent with the lobe, the PSBL and PS can extend widely in
 450 Z . So the beta condition does not reveal much about the spatial extent. In Fig. 6(b),
 451 the magnetic field condition excludes the PSBL regions, leaving the remaining PS, which
 452 is more narrow along $Z = 0$. In Fig. 6(c), the normal electric field E_z that supports the
 453 cross-tail drift current $J_y \propto -E_z B_x$ also roughly follows this spatial structure. This elec-
 454 tric field always points towards the inner PS (negative/positive in the northern/southern
 455 lobe) and tends to zero at the NS. This plot shows that the PS threshold condition agrees
 456 with the spatial structure of the PS, as drawn out by the normal electric field (E_z) and
 457 equatorial magnetic field (B_{xy}).

458 The spatial extent of E_z in the Z direction seemingly flares up to $\sim 8\text{--}10 R_E$ be-
 459 yond $|X| \gtrsim 20 R_E$, but while at closer distances, its structure is mainly located within $5 R_E$
 460 of the equator. This flaring in the Z direction of the plasma sheet can be explained with
 461 variations in the Y direction caused by the dipole tilt. Fig. 7 shows (a) the magnetospheric
 462 B_x component and (b) the dipole tilt angle Ψ in the $Y-Z$ plane. The two lobes are clearly distinguish-
 463 able in (a). In Fig. 7(a), the two lobes are clearly distinguishable, with $B_x > 0$ indicating
 464 the northern hemisphere and $B_x < 0$ indicating the southern hemisphere. The null point

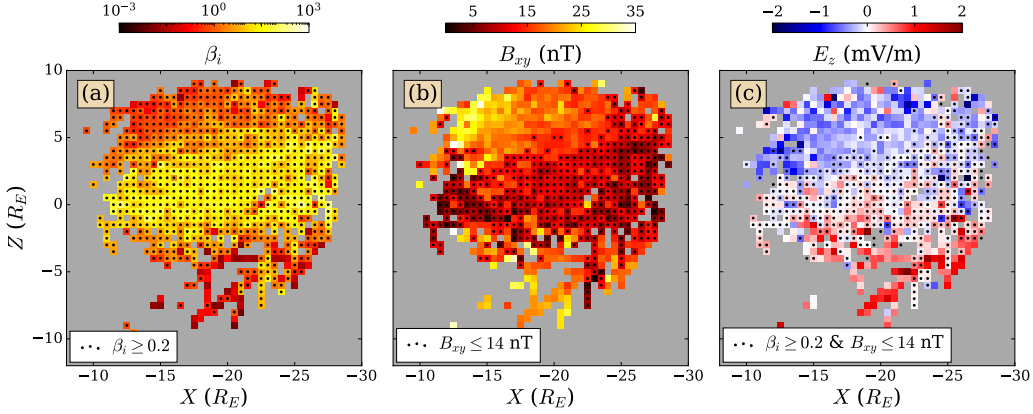


Figure 6. Spatial distribution in the X - Z plane of (a) β_i , (b) B_{xy} , and (c) E_z . In (a), marked bins (those with a circle marker at the center) satisfy the PS beta condition $\beta_i \geq 0.2$ in Table 1. Similarly, the marked bins satisfy the PS field condition $B_{xy} \leq 14$ nT in (b). Those in (c) satisfy both, the full PS condition.

B_x ∼ 0 is the location of the neutral sheet. In (b), the distribution of Ψ also reflects the aforementioned dawn-dusk asymmetry in Fig. 5, where Ψ varies between 10° and 30° in the dawn sector ($Y < 0$) and between -10° and 10° in the dusk sector ($Y > 0$).

References

- Amit, H., & Olson, P. (2008, feb). Geomagnetic dipole tilt changes induced by core flow. *Physics of the Earth and Planetary Interiors*, 166(3-4), 226–238. Retrieved from <https://linkinghub.elsevier.com/retrieve/pii/S0031920108000253> doi: 10.1016/j.pepi.2008.01.007
- Angelopoulos, V., Kennel, C. F., Coroniti, F. V., Pellat, R., Kivelson, M. G., Walker, R. J., ... Gosling, J. T. (1994). Statistical characteristics of bursty bulk flow events. *Journal of Geophysical Research*, 99(A11), 21257. Retrieved from <http://doi.wiley.com/10.1029/94JA01263> doi: 10.1029/94JA01263
- Angelopoulos, V., Sibeck, D., Carlson, C. W., McFadden, J. P., Larson, D., Lin, R. P., ... Sigwarth, J. (2008, dec). First Results from the THEMIS Mission. *Space Science Reviews*, 141(1-4), 453–476. Retrieved from <http://link.springer.com/10.1007/s11214-008-9378-4> doi: 10.1007/s11214-008-9378-4
- Artemyev, A., Lu, S., El-Alaoui, M., Lin, Y., Angelopoulos, V., Zhang, X., ...

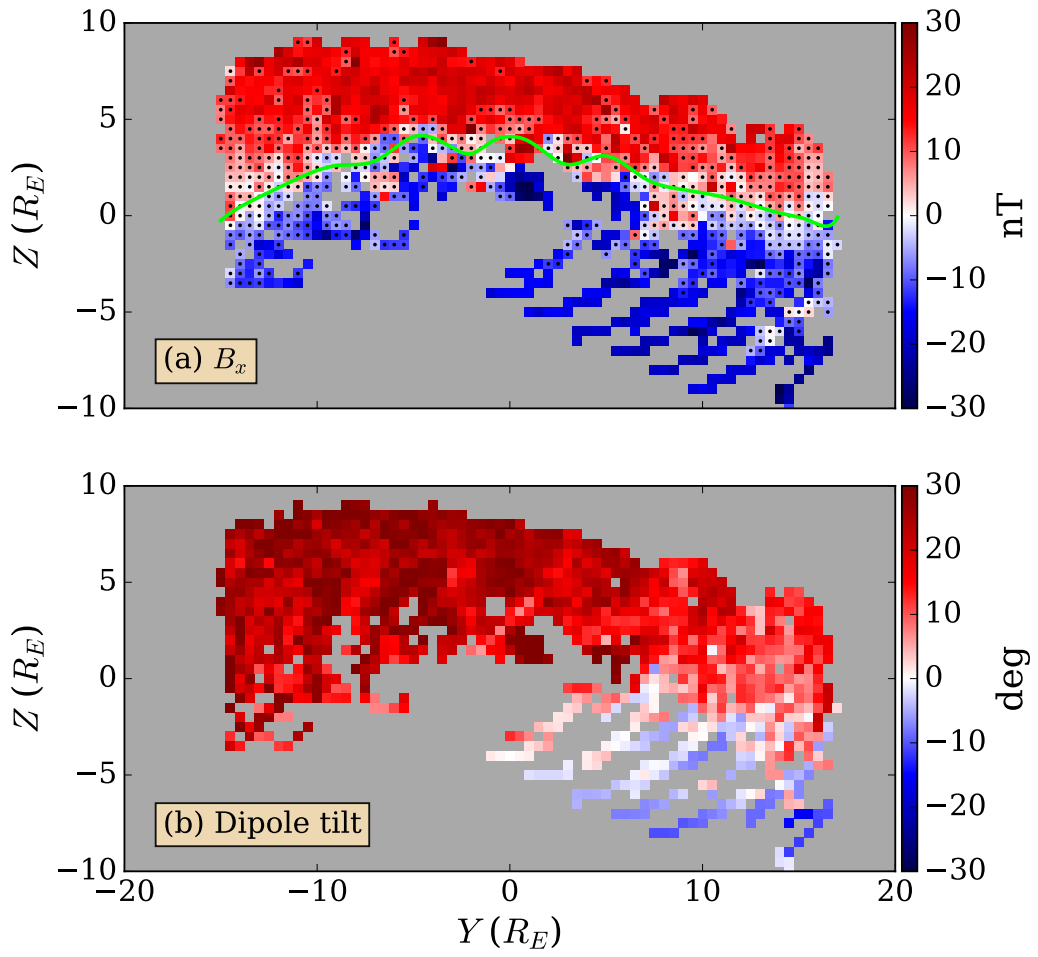


Figure 7. Spatial distribution in the Y - Z plane of (a) B_x and (b) the dipole tilt angle Ψ . The solid lime line in (a) is a global tail neutral sheet model (Xiao et al., 2016) dependent on Ψ and the average solar wind pressure $P_{\text{sw}} = 2 \text{ nPa}$. Similar to Fig. 6(c), the marked bins satisfy the plasma sheet condition (plotted in the same format).

- 483 Russell, C. (2021, mar). Configuration of the Earth's Magnetotail Cur-
 484 rent Sheet. *Geophysical Research Letters*, 48(6), 1–9. Retrieved from
 485 <https://onlinelibrary.wiley.com/doi/10.1029/2020GL092153> doi:
 486 10.1029/2020GL092153
- 487 Åsnes, A., Friedel, R. W. H., Lavraud, B., Reeves, G. D., Taylor, M. G. G. T., &
 488 Daly, P. (2008, mar). Statistical properties of tail plasma sheet electrons
 489 above 40 keV. *Journal of Geophysical Research: Space Physics*, 113(A3), n/a–
 490 n/a. Retrieved from <http://doi.wiley.com/10.1029/2007JA012502> doi:
 491 10.1029/2007JA012502
- 492 Baumjohann, W., Paschmann, G., & Cattell, C. A. (1989, jun). Average plasma
 493 properties in the central plasma sheet. *Journal of Geophysical Research: Space
 494 Physics*, 94(A6), 6597–6606. Retrieved from <http://doi.wiley.com/10.1029/JA094iA06p06597> doi: 10.1029/JA094iA06p06597
- 496 Baumjohann, W., Paschmann, G., Sckopke, N., Cattell, C. A., & Carlson, C. W.
 497 (1988). Average ion moments in the plasma sheet boundary layer. *Jour-
 498 nal of Geophysical Research*, 93(A10), 11507. Retrieved from <http://doi.wiley.com/10.1029/JA093iA10p11507> doi: 10.1029/JA093iA10p11507
- 500 Blake, J. B., Mauk, B. H., Baker, D. N., Carranza, P., Clemons, J. H., Craft,
 501 J. V., ... Westlake, J. (2016, mar). The Fly's Eye Energetic Parti-
 502 cle Spectrometer (FEEPS) Sensors for the Magnetospheric Multiscale
 503 (MMS) Mission. *Space Science Reviews*, 199(1-4), 309–329. Retrieved
 504 from <http://link.springer.com/10.1007/s11214-015-0163-x> doi:
 505 10.1007/s11214-015-0163-x
- 506 Boakes, P. D., Nakamura, R., Volwerk, M., & Milan, S. E. (2014, aug). ECLAT
 507 Cluster Spacecraft Magnetotail Plasma Region Identifications (2001–
 508 2009). *Dataset Papers in Science*, 2014, 1–13. Retrieved from <https://www.hindawi.com/journals/dpis/2014/684305/> doi: 10.1155/2014/684305
- 510 Burch, J., Moore, T. E., Torbert, R. B., & Giles, B. L. (2016, mar). Magnetospheric
 511 Multiscale Overview and Science Objectives. *Space Science Reviews*, 199(1-4),
 512 5–21. Retrieved from <http://link.springer.com/10.1007/s11214-015-0164>
 513 –9 doi: 10.1007/s11214-015-0164-9
- 514 Cattell, C. A., Mozer, F. S., Hones, E. W., Anderson, R. R., & Sharp, R. D. (1986).
 515 ISEE observations of the plasma sheet boundary, plasma sheet, and neutral

- sheet: 1. Electric field, magnetic field, plasma, and ion composition. *Journal of Geophysical Research*, 91(A5), 5663. Retrieved from <http://doi.wiley.com/10.1029/JA091iA05p05663> doi: 10.1029/JA091iA05p05663
- Chasapis, A., Yang, Y., Matthaeus, W. H., Parashar, T. N., Haggerty, C. C., Burch, J., ... Russell, C. T. (2018, jul). Energy Conversion and Collisionless Plasma Dissipation Channels in the Turbulent Magnetosheath Observed by the Magnetospheric Multiscale Mission. *The Astrophysical Journal*, 862(1), 32. Retrieved from <https://iopscience.iop.org/article/10.3847/1538-4357/aac775> doi: 10.3847/1538-4357/aac775
- Chen, L., Wang, S., Hesse, M., Ergun, R. E., Moore, T., Giles, B., ... Lindqvist, P. (2019, jun). Electron Diffusion Regions in Magnetotail Reconnection Under Varying Guide Fields. *Geophysical Research Letters*, 46(12), 6230–6238. Retrieved from <https://onlinelibrary.wiley.com/doi/10.1029/2019GL082393> doi: 10.1029/2019GL082393
- Chong, G. S., Pitkänen, T., Hamrin, M., & Kullen, A. (2022, apr). Dawn-Dusk Ion Flow Asymmetry in the Plasma Sheet: Interplanetary Magnetic Field By Versus Distance With Respect to the Neutral Sheet. *Journal of Geophysical Research: Space Physics*, 127(4). Retrieved from <https://onlinelibrary.wiley.com/doi/10.1029/2021JA030208> doi: 10.1029/2021JA030208
- Coroniti, F. V., & Kennel, C. F. (1972, jul). Changes in magnetospheric configuration during the substorm growth phase. *Journal of Geophysical Research*, 77(19), 3361–3370. Retrieved from <http://doi.wiley.com/10.1029/JA077i019p03361> doi: 10.1029/JA077i019p03361
- Cowley, S. (1991, jul). The structure and length of tail-associated phenomena in the solar wind downstream from the Earth. *Planetary and Space Science*, 39(7), 1039–1043. Retrieved from <https://linkinghub.elsevier.com/retrieve/pii/003206339190110V> doi: 10.1016/0032-0633(91)90110-V
- Coxon, J. C., Jackman, C. M., Freeman, M. P., Forsyth, C., & Rae, I. J. (2016, feb). Identifying the magnetotail lobes with Cluster magnetometer data. *Journal of Geophysical Research: Space Physics*, 121(2), 1436–1446. Retrieved from <https://onlinelibrary.wiley.com/doi/abs/10.1002/2015JA022020> doi: 10.1002/2015JA022020

- 549 Dayeh, M. A., Fuselier, S. A., Funsten, H. O., McComas, D. J., Ogasawara, K.,
550 Petrinec, S. M., ... Valek, P. (2015, apr). Shape of the terrestrial plasma
551 sheet in the near-Earth magnetospheric tail as imaged by the Interstel-
552 lar Boundary Explorer. *Geophysical Research Letters*, *42*(7), 2115–2122.
553 Retrieved from <http://doi.wiley.com/10.1002/2015GL063682> doi:
554 10.1002/2015GL063682
- 555 Dungey, J. W. (1965, apr). The length of the magnetospheric tail. *Journal of Geo-*
556 *physical Research*, *70*(7), 1753–1753. Retrieved from <http://doi.wiley.com/>
557 10.1029/JZ070i007p01753 doi: 10.1029/JZ070i007p01753
- 558 Dunlop, M. W., Dong, X., Wang, T., Eastwood, J. P., Robert, P., Haaland, S.,
559 ... De Keyser, J. (2021, nov). Curlometer Technique and Applications.
560 *Journal of Geophysical Research: Space Physics*, *126*(11). Retrieved from
561 <https://onlinelibrary.wiley.com/doi/10.1029/2021JA029538> doi:
562 10.1029/2021JA029538
- 563 Eastman, T. E., Frank, L. A., Peterson, W. K., & Lennartsson, W. (1984). The
564 plasma sheet boundary layer. *Journal of Geophysical Research*, *89*(A3), 1553.
565 Retrieved from <http://doi.wiley.com/10.1029/JA089iA03p01553> doi: 10
566 .1029/JA089iA03p01553
- 567 Ergun, R. E., Ahmadi, N., Kromyda, L., Schwartz, S. J., Chasapis, A., Hoilijoki, S.,
568 ... Giles, B. L. (2020a, aug). Observations of Particle Acceleration in Magnetic
569 Reconnection–driven Turbulence. *The Astrophysical Journal*, *898*(2), 154.
570 Retrieved from <https://iopscience.iop.org/article/10.3847/1538-4357/ab9ab6> doi: 10.3847/1538-4357/ab9ab6
- 572 Ergun, R. E., Ahmadi, N., Kromyda, L., Schwartz, S. J., Chasapis, A., Hoilijoki, S.,
573 ... Burch, J. (2020b, aug). Particle Acceleration in Strong Turbulence in the
574 Earth’s Magnetotail. *The Astrophysical Journal*, *898*(2), 153. Retrieved from
575 <https://iopscience.iop.org/article/10.3847/1538-4357/ab9ab5> doi:
576 10.3847/1538-4357/ab9ab5
- 577 Ergun, R. E., Andersson, L., Tao, J., Angelopoulos, V., Bonnell, J. W., McFadden,
578 J. P., ... Baumjohann, W. (2009, apr). Observations of Double Layers in
579 Earth’s Plasma Sheet. *Physical Review Letters*, *102*(15), 155002. Retrieved
580 from <https://link.aps.org/doi/10.1103/PhysRevLett.102.155002> doi:
581 10.1103/PhysRevLett.102.155002

- 582 Ergun, R. E., Goodrich, K. A., Stawarz, J. E., Andersson, L., & Angelopoulos,
 583 los, V. (2015, mar). Large-amplitude electric fields associated with
 584 bursty bulk flow braking in the Earth's plasma sheet. *Journal of Geo-*
 585 *physical Research: Space Physics*, 120(3), 1832–1844. Retrieved from
 586 <https://onlinelibrary.wiley.com/doi/10.1002/2014JA020165> doi:
 587 10.1002/2014JA020165
- 588 Ergun, R. E., Goodrich, K. A., Wilder, F. D., Ahmadi, N., Holmes, J. C., Eriksson,
 589 S., ... Vaivads, A. (2018, apr). Magnetic Reconnection, Turbu-
 590 lence, and Particle Acceleration: Observations in the Earth's Magneto-
 591 tail. *Geophysical Research Letters*, 45(8), 3338–3347. Retrieved from
 592 <https://onlinelibrary.wiley.com/doi/abs/10.1002/2018GL076993> doi:
 593 10.1002/2018GL076993
- 594 Ergun, R. E., Tucker, S., Westfall, J., Goodrich, K. A., Malaspina, D. M., Summers,
 595 D., ... Cully, C. M. (2016, mar). The Axial Double Probe and Fields Signal
 596 Processing for the MMS Mission. *Space Science Reviews*, 199(1-4), 167–188.
 597 Retrieved from <http://link.springer.com/10.1007/s11214-014-0115-x>
 598 doi: 10.1007/s11214-014-0115-x
- 599 Ergun, R. E., Usanova, M. E., Turner, D. L., & Stawarz, J. E. (2022, jun).
 600 Bursty Bulk Flow Turbulence as a Source of Energetic Particles to the Outer
 601 Radiation Belt. *Geophysical Research Letters*, 49(11). Retrieved from
 602 <https://onlinelibrary.wiley.com/doi/10.1029/2022GL098113> doi:
 603 10.1029/2022GL098113
- 604 Escoubet, C. P., Fehringer, M., & Goldstein, M. (2001, sep). The Cluster mis-
 605 sion: Introduction. *Annales Geophysicae*, 19(10/12), 1197–1200. Retrieved
 606 from <https://angeo.copernicus.org/articles/19/1197/2001/> doi:
 607 10.5194/angeo-19-1197-2001
- 608 Fairfield, D. H., Otto, A., Mukai, T., Kokubun, S., Lepping, R. P., Steinberg, J. T.,
 609 ... Yamamoto, T. (2000, sep). Geotail observations of the Kelvin-Helmholtz
 610 instability at the equatorial magnetotail boundary for parallel northward
 611 fields. *Journal of Geophysical Research: Space Physics*, 105(A9), 21159–
 612 21173. Retrieved from <http://doi.wiley.com/10.1029/1999JA000316> doi:
 613 10.1029/1999JA000316
- 614 Fuselier, S. A., Lewis, W. S., Schiff, C., Ergun, R., Burch, J., Petrinec, S. M., &

- 615 Trattner, K. J. (2016, mar). Magnetospheric Multiscale Science Mission
 616 Profile and Operations. *Space Science Reviews*, 199(1-4), 77–103. Retrieved
 617 from <https://link.springer.com/10.1007/s11214-014-0087-x> doi:
 618 10.1007/s11214-014-0087-x
- 619 Gao, J. W., Rong, Z. J., Cai, Y. H., Lui, A. T. Y., Petrukovich, A. A., Shen, C.,
 620 ... Wan, W. X. (2018, sep). The Distribution of Two Flapping Types
 621 of Magnetotail Current Sheet: Implication for the Flapping Mechanism.
 622 *Journal of Geophysical Research: Space Physics*, 123(9), 7413–7423. Retrieved
 623 from <http://doi.wiley.com/10.1029/2018JA025695> doi:
 624 10.1029/2018JA025695
- 625 Grigorenko, E. E., Koleva, R., & Sauvaud, J.-A. (2012, sep). On the problem
 626 of Plasma Sheet Boundary Layer identification from plasma moments in
 627 Earth's magnetotail. *Annales Geophysicae*, 30(9), 1331–1343. Retrieved
 628 from <https://angeo.copernicus.org/articles/30/1331/2012/> doi:
 629 10.5194/angeo-30-1331-2012
- 630 Haaland, S., Kronberg, E. A., Daly, P. W., Fränz, M., Degener, L., Georgescu, E., &
 631 Dandouras, I. (2010, aug). Spectral characteristics of protons in the Earth's
 632 plasmashell: statistical results from Cluster CIS and RAPID. *Annales Geo-*
 633 *physicae*, 28(8), 1483–1498. Retrieved from <https://angeo.copernicus.org/articles/28/1483/2010/> doi: 10.5194/angeo-28-1483-2010
- 635 Hammond, C. M., Kivelson, M. G., & Walker, R. J. (1994). Imaging the effect
 636 of dipole tilt on magnetotail boundaries. *Journal of Geophysical Research*,
 637 99(A4), 6079. Retrieved from <http://doi.wiley.com/10.1029/93JA01924>
 638 doi: 10.1029/93JA01924
- 639 Henderson, M., Morley, S., Niehof, J., & Larsen, B. A. (2018). *LANLGeoMag*. Zen-
 640 odo. Retrieved from <https://doi.org/10.5281/zenodo.1195041> doi: 10
 641 .5281/zenodo.1195041
- 642 Hietala, H., Drake, J. F., Phan, T. D., Eastwood, J. P., & McFadden, J. P.
 643 (2015, sep). Ion temperature anisotropy across a magnetotail reconnec-
 644 tion jet. *Geophysical Research Letters*, 42(18), 7239–7247. Retrieved from
 645 <https://onlinelibrary.wiley.com/doi/10.1002/2015GL065168> doi:
 646 10.1002/2015GL065168
- 647 Huang, S. Y., Wei, Y. Y., Yuan, Z. G., Jiang, K., Deng, X. H., Xu, S. B., ... Zhang,

- 648 Z. H. (2020). Electron Jets in the Terrestrial Magnetotail: A Statistical
649 Overview. *The Astrophysical Journal*, 896(1), 67. doi: 10.3847/1538-4357/
650 ab8eb0
- 651 Johnson, J. R., Wing, S., & Delamere, P. A. (2014, nov). Kelvin Helmholtz Instabil-
652 ity in Planetary Magnetospheres. *Space Science Reviews*, 184(1-4), 1–31. Re-
653 tried from <http://link.springer.com/10.1007/s11214-014-0085-z> doi:
654 10.1007/s11214-014-0085-z
- 655 King, J. H., & Papitashvili, N. E. (2005). Solar wind spatial scales in and com-
656 parisons of hourly Wind and ACE plasma and magnetic field data. *Journal*
657 *of Geophysical Research*, 110(A2), A02104. Retrieved from <http://doi.wiley.com/10.1029/2004JA010649> doi: 10.1029/2004JA010649
- 659 Lin, R. L., Zhang, X. X., Liu, S. Q., Wang, Y. L., & Gong, J. C. (2010, apr). A
660 three-dimensional asymmetric magnetopause model. *Journal of Geophysical*
661 *Research: Space Physics*, 115(A4). Retrieved from <http://doi.wiley.com/10.1029/2009JA014235> doi: 10.1029/2009JA014235
- 663 Liu, Y., Birn, J., Daughton, W., Hesse, M., & Schindler, K. (2014, dec). On-
664 set of reconnection in the near magnetotail: PIC simulations. *Journal of*
665 *Geophysical Research: Space Physics*, 119(12), 9773–9789. Retrieved from
666 <https://onlinelibrary.wiley.com/doi/10.1002/2014JA020492> doi:
667 10.1002/2014JA020492
- 668 Lui, A. T. Y., Meng, C.-I., & Akasofu, S.-I. (1978, apr). Wavy nature of the
669 magnetotail neutral sheet. *Geophysical Research Letters*, 5(4), 279–282.
670 Retrieved from <http://doi.wiley.com/10.1029/GL005i004p00279> doi:
671 10.1029/GL005i004p00279
- 672 Malaspina, D. M., Wygant, J. R., Ergun, R. E., Reeves, G. D., Skoug, R. M., &
673 Larsen, B. A. (2015, jun). Electric field structures and waves at plasma bound-
674 aries in the inner magnetosphere. *Journal of Geophysical Research: Space*
675 *Physics*, 120(6), 4246–4263. Retrieved from <https://onlinelibrary.wiley.com/doi/10.1002/2015JA021137> doi: 10.1002/2015JA021137
- 677 Mauk, B. H., Blake, J. B., Baker, D. N., Clemmons, J. H., Reeves, G. D., Spence,
678 H. E., ... Westlake, J. H. (2016, mar). The Energetic Particle Detector (EPD)
679 Investigation and the Energetic Ion Spectrometer (EIS) for the Magnetospheric
680 Multiscale (MMS) Mission. *Space Science Reviews*, 199(1-4), 471–514. Re-

- trieved from <http://link.springer.com/10.1007/s11214-014-0055-5> doi:
10.1007/s11214-014-0055-5
- McComas, D. J., Russell, C. T., Elphic, R. C., & Bame, S. J. (1986). The near-Earth cross-tail current sheet: Detailed ISEE 1 and 2 case studies. *Journal of Geophysical Research*, 91(A4), 4287. Retrieved from <http://doi.wiley.com/10.1029/JA091iA04p04287> doi: 10.1029/JA091iA04p04287
- Nakamura, R., Baumjohann, W., Nagai, T., Fujimoto, M., Mukai, T., Klecker, B., ... Bogdanova, Y. (2004). Flow shear near the boundary of the plasma sheet observed by Cluster and Geotail. *Journal of Geophysical Research*, 109(A5), A05204. Retrieved from <http://doi.wiley.com/10.1029/2003JA010174> doi: 10.1029/2003JA010174
- Nykyri, K., Otto, A., Lavraud, B., Mouikis, C., Kistler, L. M., Balogh, A., & Rème, H. (2006, oct). Cluster observations of reconnection due to the Kelvin-Helmholtz instability at the dawnside magnetospheric flank. *Annales Geophysicae*, 24(10), 2619–2643. Retrieved from <https://angeo.copernicus.org/articles/24/2619/2006/> doi: 10.5194/angeo-24-2619-2006
- Otto, A., & Fairfield, D. H. (2000, sep). Kelvin-Helmholtz instability at the magnetotail boundary: MHD simulation and comparison with Geotail observations. *Journal of Geophysical Research: Space Physics*, 105(A9), 21175–21190. Retrieved from <http://doi.wiley.com/10.1029/1999JA000312> doi: 10.1029/1999JA000312
- Owen, C. J., Slavin, J. A., Richardson, I. G., Murphy, N., & Hynds, R. J. (1995). Average motion, structure and orientation of the distant magnetotail determined from remote sensing of the edge of the plasma sheet boundary layer with $E > 35$ keV ions. *Journal of Geophysical Research*, 100(A1), 185. Retrieved from <http://doi.wiley.com/10.1029/94JA02417> doi: 10.1029/94JA02417
- Paschmann, G., & Daly, P. (1998). *Analysis Methods for Multi-Spacecraft Data*.
- Pedersen, A., Cattell, C. A., Fälthammar, C.-G., Knott, K., Lindqvist, P.-A., Manka, R. H., & Mozer, F. S. (1985). Electric fields in the plasma sheet and plasma sheet boundary layer. *Journal of Geophysical Research*, 90(A2), 1231. Retrieved from <http://doi.wiley.com/10.1029/JA090iA02p01231> doi: 10.1029/JA090iA02p01231

- 714 Pollock, C., Moore, T., Jacques, A., Burch, J., Gliese, U., Saito, Y., ... Zeuch, M.
 715 (2016, mar). Fast Plasma Investigation for Magnetospheric Multiscale. *Space*
 716 *Science Reviews*, 199(1-4), 331–406. Retrieved from <http://link.springer.com/10.1007/s11214-016-0245-4> doi: 10.1007/s11214-016-0245-4
- 717 Rong, Z. J., Cai, Y. H., Gao, J. W., Lui, A. T. Y., Shen, C., Petrukovich, A. A.,
 718 ... Wan, W. X. (2018, jul). Cluster Observations of a Dispersive Flapping
 719 Event of Magnetotail Current Sheet. *Journal of Geophysical Research: Space*
 720 *Physics*, 123(7), 5571–5579. Retrieved from <http://doi.wiley.com/10.1029/2018JA025196> doi: 10.1029/2018JA025196
- 721 Runov, A., Angelopoulos, V., Sergeev, V. A., Glassmeier, K.-H., Auster, U., Mc-
 722 Fadden, J., ... Mann, I. (2009, jan). Global properties of magnetotail current
 723 sheet flapping: THEMIS perspectives. *Annales Geophysicae*, 27(1), 319–328.
 724 Retrieved from <https://angeo.copernicus.org/articles/27/319/2009/>
 725 doi: 10.5194/angeo-27-319-2009
- 726 Runov, A., Sergeev, V. A., Baumjohann, W., Nakamura, R., Apatenkov, S., Asano,
 727 ... Rème, H. (2005, jun). Electric current and magnetic field geometry in
 728 flapping magnetotail current sheets. *Annales Geophysicae*, 23(4), 1391–1403.
 729 Retrieved from <https://angeo.copernicus.org/articles/23/1391/2005/>
 730 doi: 10.5194/angeo-23-1391-2005
- 731 Russell, C. T., Anderson, B. J., Baumjohann, W., Bromund, K. R., Dearborn,
 732 D., Fischer, D., ... Richter, I. (2016, mar). The Magnetospheric Multi-
 733 scale Magnetometers. *Space Science Reviews*, 199(1-4), 189–256. Retrieved
 734 from <http://link.springer.com/10.1007/s11214-014-0057-3> doi:
 735 10.1007/s11214-014-0057-3
- 736 Russell, C. T., & McPherron, R. L. (1973). The magnetotail and substorms. *Space*
 737 *Science Reviews*, 15(2-3), 205–266. Retrieved from <http://link.springer.com/10.1007/BF00169321> doi: 10.1007/BF00169321
- 738 Sanny, J., McPherron, R. L., Russell, C. T., Baker, D. N., Pulkkinen, T. I., &
 739 Nishida, A. (1994). Growth-phase thinning of the near-Earth current sheet
 740 during the CDAW 6 substorm. *Journal of Geophysical Research*, 99(A4),
 741 5805. Retrieved from <http://doi.wiley.com/10.1029/93JA03235> doi:
 742 10.1029/93JA03235
- 743 Sergeev, V., Runov, A., Baumjohann, W., Nakamura, R., Zhang, T. L., Volw-

- 747 erk, M., ... Klecker, B. (2003, mar). Current sheet flapping motion and
 748 structure observed by Cluster. *Geophysical Research Letters*, *30*(6), 2–
 749 5. Retrieved from <http://doi.wiley.com/10.1029/2002GL016500> doi:
 750 10.1029/2002GL016500
- 751 Shukhtina, M. A., Dmitrieva, N. P., & Sergeev, V. A. (2004, mar). Quantitative
 752 magnetotail characteristics of different magnetospheric states. *Annales Geo-*
 753 *physicae*, *22*(3), 1019–1032. Retrieved from <https://angeo.copernicus.org/articles/22/1019/2004/> doi: 10.5194/angeo-22-1019-2004
- 755 Shustov, P. I., Zhang, X., Pritchett, P. L., Artemyev, A., Angelopoulos, V.,
 756 Yushkov, E. V., & Petrukovich, A. A. (2019, jan). Statistical Properties of
 757 Sub-Ion Magnetic Holes in the Dipolarized Magnetotail: Formation, Struc-
 758 ture, and Dynamics. *Journal of Geophysical Research: Space Physics*, *124*(1),
 759 342–359. Retrieved from <https://onlinelibrary.wiley.com/doi/10.1029/2018JA025852> doi: 10.1029/2018JA025852
- 761 Sitnov, M., Birn, J., Ferdousi, B., Gordeev, E., Khotyaintsev, Y., Merkin, V., ...
 762 Zhou, X. (2019, jun). Explosive Magnetotail Activity. *Space Science Re-*
 763 *views*, *215*(4), 31. Retrieved from <http://link.springer.com/10.1007/s11214-019-0599-5> doi: 10.1007/s11214-019-0599-5
- 765 Sitnov, M., & Schindler, K. (2010, apr). Tearing stability of a multiscale mag-
 766 netotail current sheet. *Geophysical Research Letters*, *37*(8), 1–5. Re-
 767 tried from <http://doi.wiley.com/10.1029/2010GL042961> doi:
 768 10.1029/2010GL042961
- 769 Tedla, Y. T., Davis, G., & Arocho, R. (2018, may). Magnetospheric Multiscale
 770 (MMS) Mission: Surviving Extended Mission Long Eclipse. In *2018 spaceops*
 771 *conference*. Reston, Virginia: American Institute of Aeronautics and Astronautics.
 772 Retrieved from <https://arc.aiaa.org/doi/10.2514/6.2018-2389> doi:
 773 10.2514/6.2018-2389
- 774 Tong, Y., Vasko, I., Mozer, F. S., Bale, S. D., Roth, I., Artemyev, A., ... Torbert,
 775 R. B. (2018, nov). Simultaneous Multispacecraft Probing of Electron Phase
 776 Space Holes. *Geophysical Research Letters*, *45*(21), 11,513–11,519. Retrieved
 777 from <https://onlinelibrary.wiley.com/doi/10.1029/2018GL079044> doi:
 778 10.1029/2018GL079044
- 779 Torbert, R. B., Russell, C. T., Magnes, W., Ergun, R. E., Lindqvist, P.-A., LeCon-

- 780 tel, O., ... Lappalainen, K. (2016, mar). The FIELDS Instrument Suite on
 781 MMS: Scientific Objectives, Measurements, and Data Products. *Space Science*
 782 *Reviews*, 199(1-4), 105–135. Retrieved from <http://link.springer.com/10.1007/s11214-014-0109-8> doi: 10.1007/s11214-014-0109-8
- 783
- 784 Tsyganenko, N. A. (1998, oct). Modeling of twisted/warped magnetospheric
 785 configurations using the general deformation method. *Journal of Geo-*
 786 *physical Research: Space Physics*, 103(A10), 23551–23563. Retrieved from
 787 <http://doi.wiley.com/10.1029/98JA02292> doi: 10.1029/98JA02292
- 788 Tsyganenko, N. A., & Fairfield, D. H. (2004). Global shape of the magnetotail cur-
 789 rent sheet as derived from Geotail and Polar data. *Journal of Geophysical Re-*
 790 *search*, 109(A3), A03218. Retrieved from <http://doi.wiley.com/10.1029/2003JA010062> doi: 10.1029/2003JA010062
- 791
- 792 Ukhorskiy, A. Y., Sitnov, M. I., Merkin, V. G., Gkioulidou, M., & Mitchell, D. G.
 793 (2017, mar). Ion acceleration at dipolarization fronts in the inner magne-
 794 tosphere. *Journal of Geophysical Research: Space Physics*, 122(3), 3040–
 795 3054. Retrieved from <https://onlinelibrary.wiley.com/doi/10.1002/2016JA023304> doi: 10.1002/2016JA023304
- 796
- 797 Usanova, M. E., & Ergun, R. E. (2022). Electron Energization by High-Amplitude
 798 Turbulent Electric Fields: A Possible Source of the Outer Radiation
 799 Belt. *Journal of Geophysical Research: Space Physics*(2015), 1–16. doi:
 800 10.1029/2022ja030336
- 801
- 802 Wang, G. Q., Zhang, T. L., Wu, M. Y., Schmid, D., Cao, J. B., & Volwerk, M.
 803 (2019, jan). Solar Wind Directional Change Triggering Flapping Motions
 804 of the Current Sheet: MMS Observations. *Geophysical Research Letters*,
 805 46(1), 64–70. Retrieved from <https://onlinelibrary.wiley.com/doi/abs/10.1029/2018GL080023> doi: 10.1029/2018GL080023
- 806
- 807 Xiao, S., Zhang, T., Ge, Y., Wang, G., Baumjohann, W., & Nakamura, R.
 808 (2016, feb). A statistical study on the shape and position of the magne-
 809 totail neutral sheet. *Annales Geophysicae*, 34(2), 303–311. Retrieved
 810 from <https://angeo.copernicus.org/articles/34/303/2016/> doi:
 10.5194/angeo-34-303-2016
- 811
- 812 Yang, Y., Matthaeus, W. H., Roy, S., Roytershteyn, V., Parashar, T. N., Bandy-
 opadhyay, R., & Wan, M. (2022, apr). Pressure–Strain Interaction as the

- 813 Energy Dissipation Estimate in Collisionless Plasma. *The Astrophysical Journal*,
814 929(2), 142. Retrieved from <https://iopscience.iop.org/article/10.3847/1538-4357/ac5d3e> doi: 10.3847/1538-4357/ac5d3e
- 815 Zenitani, S., & Hoshino, M. (2005, jan). Relativistic Particle Acceleration in a
816 Folded Current Sheet. *The Astrophysical Journal*, 618(2), L111–L114. Re-
trieved from <https://iopscience.iop.org/article/10.1086/427873> doi:
817 10.1086/427873
- 818 Zhang, T. L., Nakamura, R., Volwerk, M., Runov, A., Baumjohann, W., Eichel-
819 berger, H. U., ... Fornacon, K.-H. (2005, nov). Double Star/Cluster observation
820 of neutral sheet oscillations on 5 August 2004. *Annales Geophysicae*, 23(8),
821 2909–2914. Retrieved from <https://angeo.copernicus.org/articles/23/2909/2005/> doi: 10.5194/angeo-23-2909-2005
- 822 Zhou, X., Russell, C. T., Gosling, J. T., & Mitchell, D. G. (1997, jan). Three
823 spacecraft observations of the geomagnetic tail during moderately disturbed
824 conditions: Structure and evolution of the current sheet. *Journal of Geo-
825 physical Research: Space Physics*, 102(A7), 14415–14424. Retrieved from
826 <https://onlinelibrary.wiley.com/doi/abs/10.1029/97JA00038> doi:
827 10.1029/97JA00038
- 828 Zimbardo, G., Greco, A., Sorriso-Valvo, L., Perri, S., Vörös, Z., Aburjania, G.,
829 ... Alexandrova, O. (2010, oct). Magnetic Turbulence in the Geospace
830 Environment. *Space Science Reviews*, 156(1-4), 89–134. Retrieved
831 from <http://link.springer.com/10.1007/s11214-010-9692-5> doi:
832 10.1007/s11214-010-9692-5
- 833
- 834
- 835